

# Highly Conductive Freestanding Graphene Films as Anode Current Collectors for Flexible Lithium-Ion Batteries

Kuldeep Rana,<sup>†</sup> Jyoti Singh,<sup>†</sup> Jeong-Taik Lee,<sup>‡</sup> Jong Hyeok Park,<sup>\*,‡</sup> and Jong-Hyun Ahn<sup>\*,†</sup>

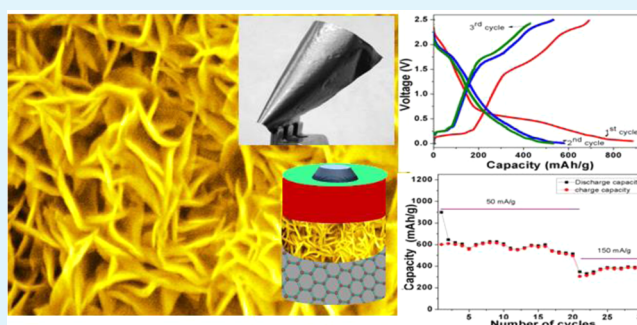
<sup>†</sup>School of Electrical and Electronic Engineering, Yonsei University, Seoul, 120-749, Korea

<sup>‡</sup>School of Chemical Engineering, Sungkyunkwan University, Suwon, 440-746, Korea

## Supporting Information

**ABSTRACT:** The electrodes in lithium-ion batteries (LIBs) are typically films that are arranged on metal foil current collectors with a thickness of several tens of  $\mu\text{m}$ . Here, we report on the preparation of a thick free-standing graphene film synthesized by CVD as an alternative to Cu foil as an anode current collector. As a model system, MoS<sub>2</sub> anodes with a flower-like morphology were anchored onto the surface of the thick graphene film. A hybrid and binder free anode without a conventional metal current collector exhibited an excellent capacity value of around 580 mAh/g (@50 mA/g) and reasonable charge/discharge cyclability. The work presented here may stimulate the use of graphene films as replacements for conventional current collectors and additive free electrode in LIBs.

**KEYWORDS:** flexible current collector, CVD, binder-free electrode, graphene, MoS<sub>2</sub>, Li-ion battery



## INTRODUCTION

Lithium-ion batteries (LIBs) are increasingly used as energy sources in portable electronic devices and represent attractive power sources for electric transport vehicles in the near future. A variety of carbonaceous materials have been utilized in commercial LIBs due to their high structural stability, flat voltage profile, good electronic conductivity, and low-cost preparation. However, carbonaceous materials are limited by their low theoretical specific capacity of 372 mAh/g.<sup>1</sup> Graphene, which is essentially a monolayer of graphite, is an attractive energy storage material<sup>2,3</sup> for use in lithium-ion batteries as it exhibits excellent electronic properties, good mechanical flexibility, and a very high surface area that facilitates lithium-ion uptake, which in turn increases the specific capacity.<sup>4,5</sup> Numerous efforts have been applied towards developing different types of graphene-based anode materials, including reduced graphene oxide,<sup>6</sup> graphene paper,<sup>7</sup> porous graphene,<sup>8,9</sup> graphene networks,<sup>10,11</sup> and heteroatom-doped graphene.<sup>10–12</sup> Moreover, several of the drawbacks that hinder the performance of high-capacity materials (e.g., metal oxides and sulfides), including low conductivity and poor long-term cyclability because of volume expansion and pulverization during charging and discharging, have been mitigated with the introduction of graphene.<sup>13–15</sup>

Recently, bendable and rollable electronic devices (e.g., rollup and wearable displays) have garnered extensive interest from the research community. However, a major obstacle to the realization of bendable energy storage devices is the lack of reliable materials that have superior electrical conductivity, high mechanical flexibility, and high electrochemical stability. Metal

foils have been employed as current collectors in conventional LIBs, but their high cost, high weight, and low flexibility have led to the exploration of alternative materials. To replace conventional metal foil current collectors, graphene flakes have been utilized for both the cathode and anode in flexible LIBs.<sup>7</sup> However, the electrical properties of graphene films made from graphene flakes are insufficient for use in LIBs. Therefore, alternative graphene materials with suitable mechanical flexibility, electrical properties, and electrochemical stability must be investigated. Such materials must act not only as a conducting agent, but also as a current collector.

In the present work, we describe a facile two-step synthesis process for the preparation of a thick freestanding graphene film (FSG) coated with a model anode material (MoS<sub>2</sub>)<sup>16</sup> for LIBs without the use of a polymer binder or conducting agent. The proposed strategy can reduce the cost and total weight of the cell, while increasing the flexibility of LIBs. The presence of a binder (10–12% total weight of the electrode) can decrease the capacity during longer cycles and induce thermal runaway at elevated temperatures.<sup>17</sup> Electrode materials with a polymer binder have always required extra safety features when incorporated into the batteries. Binder-free electrodes would eliminate the need for such additional procedures, while avoiding the use of a metallic current collector will reduce the weight of the battery. The effective strategy proposed in this manuscript may provide new insights into the fabrication of

Received: February 17, 2014

Accepted: April 22, 2014

Published: April 23, 2014

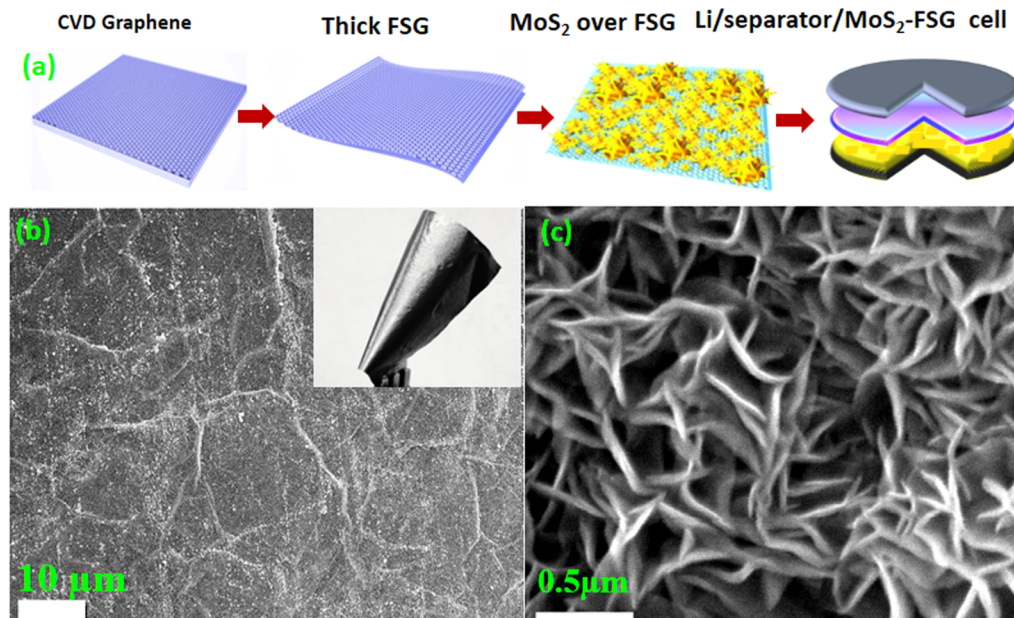


**Figure 1.** (a) Schematic illustration of the synthesis procedure for thick FSG/MoS<sub>2</sub> films. Step 1: thick FSG grown on a Ni substrate by the CVD method. Step 2: FSG film after etching of the Ni. Step 3: MoS<sub>2</sub> growth over FSG by the hydrothermal method at 200 °C. Step 4: fabrication of a coin cell with an FSG/MoS<sub>2</sub> electrode. A cross-sectional view of the coin cell used for electrochemical testing is shown. (b) FE-SEM image of the FSG surface; a photograph of a flexible FSG film is displayed in the inset. (c) Microstructure of the as-synthesized MoS<sub>2</sub> on FSG; uniform growth and a vertical petal-like morphology are evident.

hybrid electrodes for safe, high-performance LIBs. Here, we synthesized thick graphene films on Ni substrates. The Ni substrates were subsequently etched away to provide free-standing thick graphene films that could be used directly as both a current collector and a support for MoS<sub>2</sub> grown via the hydrothermal method.

## RESULTS AND DISCUSSION

A schematic of the fabrication process for FSG/MoS<sub>2</sub> hybrid electrodes is shown in Figure 1a. Our synthesis strategy begins with the growth of a thick graphene film over Ni using the CVD method; the thickness of the graphene film is approximately 8 μm (step 1 of Figure 1a). The formation of a crystalline, thick freestanding graphene film is a process of considerable interest from a scientific and technological point of view. Polycrystalline Ni films (thickness = 25 μm), which served as metal catalysts to grow thick graphene films, were first annealed at 1000 °C in an Ar/H<sub>2</sub> atmosphere, which increases the grain size of the Ni. The films were then exposed to an H<sub>2</sub>/CH<sub>4</sub> gas mixture under ambient pressure. Decomposition of the CH<sub>4</sub> ensues and carbon atoms dissolve into the Ni film through grain boundaries, leading to the formation of a Ni–C solid solution (max. solubility 2.7 at %). Carbon atoms ultimately diffuse out from the Ni–C solid solution and precipitate on the Ni surface after fast cooling to form a graphene film. Grain boundaries act as favorable sites for the nucleation of graphene due to the local change in structure at grain boundary intersections, while also serving as preferred routes for the diffusion of carbon due to the effect of localized impurity concentrations as a result of segregation to the boundary. The graphene films grown on Ni substrates are continuous and consist of thousands of layers that cover the entire substrate surface. After chemical etching of the Ni, a thick FSG film was obtained (step 2 of Figure 1a). FSG was used as a base material on which MoS<sub>2</sub> was grown via the

hydrothermal method (step 3 of Figure 1a). Ultimately, three-dimensional hybrid architectures are obtained. All required chemicals ((NH<sub>4</sub>)<sub>2</sub>MoO<sub>4</sub>, CS(NH<sub>2</sub>)<sub>2</sub>, and NH<sub>2</sub>NH<sub>2</sub>) were mixed in water and transferred to the hydrothermal vessel together with the FSG films. During the hydrothermal process, MoO<sub>4</sub><sup>2-</sup> anions that adsorbed onto the FSG surface were reduced and sulfurized by hydrazine and thiourea in solution after heating at 200 °C, leading to the formation of a FSG/MoS<sub>2</sub> hybrid structure. During the reaction, H<sub>2</sub>S was released in situ from thiourea at high temperature and reacted with MoO<sub>4</sub><sup>2-</sup> species to yield MoS<sub>2</sub>. The as-synthesized hybrid FSG/MoS<sub>2</sub> structure was a freestanding film that could be directly used as a battery anode without any post-processing or the need for additives (e.g., polymer binder, carbon black). The cross-sectional view of the coin cell structure used for electrochemical testing shows the different layers consisting of the lithium metal foil, the separator (polypropylene film), and the hybrid electrode (FSG/MoS<sub>2</sub>) to be tested (step 4 of Figure 1a). A FE-SEM image of the thick FSG film surface after removing the Ni is shown in Figure 1b; a morphology of large grains separated by grain boundaries is clearly evident. An image of the thick FSG film after nickel etching is displayed in the inset of Figure 1b, while the resistance of the FSG film at different bending radii is shown in Figure S1b in the Supporting Information. The FSG film retains its electrical properties even at a bending radius of less than 2 mm. This indicates that the films are flexible and bendable without any deformation, i.e., the materials are mechanically robust. The growth of MoS<sub>2</sub> was confirmed using various characterization techniques. Figure S1a in the Supporting Information reveals that MoS<sub>2</sub> was grown uniformly over the majority of the thick FSG surface and thus, the structure could be used directly as an electrode in a coin cell without any further processing. A more detailed view of the MoS<sub>2</sub> morphology with flower-type nanostructures is shown in the higher magnification images of Figure 1c; isolated, vertically

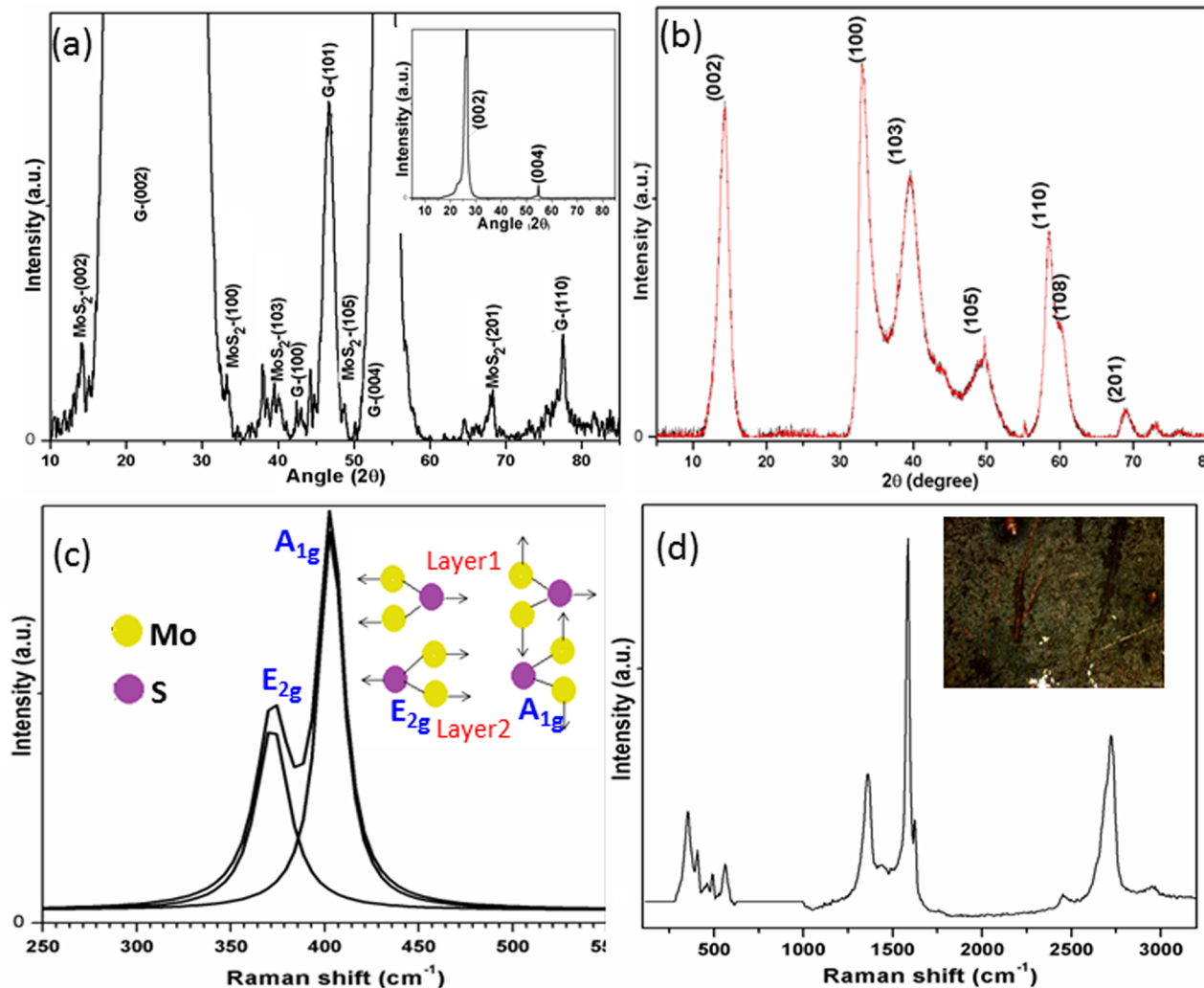


**Figure 2.** (a) XRD pattern of MoS<sub>2</sub>/FSG hybrid structure shows the 2H-MoS<sub>2</sub> peaks together with graphite peaks and inset shows the FSG film without MoS<sub>2</sub>. (b) XRD pattern of MoS<sub>2</sub> powder synthesized during hydrothermal reaction showed well crystallized stacked 2H-MoS<sub>2</sub> (c) Detail of peaks in Raman spectrum of MoS<sub>2</sub> shows two different vibration modes and (d) Raman spectra of MoS<sub>2</sub>/FSG after cell testing for 20th cycle, the inset shows the optical image of the same.

oriented MoS<sub>2</sub> nanowalls are clearly evident. The wall thickness, as measured using ImageJ, was found to be in the range of 30–40 nm with a gap of a few nanometres. Each nanowall consisted of several thin nanosheets of MoS<sub>2</sub> that had agglomerated during growth, leading to the formation of a flower-like morphology.<sup>18</sup> The morphology of the 3D FSG/MoS<sub>2</sub>-based hybrid structures, when used as anode materials, provides a large surface area for good electrode–electrolyte interaction and facilitates smooth charge transfer from the MoS<sub>2</sub> to the FSG.

The XRD pattern of a FSG/MoS<sub>2</sub> film is shown in Figure 2a; the pattern of a thick FSG film before MoS<sub>2</sub> growth is displayed in the inset. The FSG synthesized by CVD exhibited a high degree of crystallinity with intense XRD peaks, and primary reflections from graphite (002) and (004) planes are clearly observed. The MoS<sub>2</sub> peaks were weaker in intensity and showed lower crystallinity when compared to the FSG reflections. Upon annealing at 500 °C, sharp graphite and MoS<sub>2</sub> diffraction peaks are seen after zooming in on the y-axis; the intensities of the MoS<sub>2</sub> peaks are lower than those of the FSG reflections. The presence of most of the MoS<sub>2</sub> diffraction peaks in the XRD pattern confirmed the growth of 2H-MoS<sub>2</sub>.

on the thick graphene surface. The main diffraction peak appearing at  $2\theta = 14.2^\circ$  with a *d*-spacing of 6.2 Å implies the existence of a well-stacked layered structure and demonstrates that crystalline MoS<sub>2</sub> was formed. Figure 2b shows the XRD pattern of MoS<sub>2</sub> powder synthesized during the hydrothermal synthesis of FSG/MoS<sub>2</sub> which indicates that all the diffraction peaks can be indexed as hexagonal 2H-MoS<sub>2</sub> identical to the reported data without the presence of any impurity phase. The Raman spectra of pure FSG and FSG after the growth of MoS<sub>2</sub> by the hydrothermal method are shown in Figure S2a in the Supporting Information. In the Raman spectrum of FSG, the most intense features appeared at 1573  $\text{cm}^{-1}$  (G-band) due to the in-plane vibrations of carbon atoms (also known as the E<sub>2g</sub> mode). Furthermore, a peak appeared at 1345  $\text{cm}^{-1}$  (D-band) due to the presence of defects in the carbon lattice, while the G'-band at 2685  $\text{cm}^{-1}$  is related to a second-order Raman process.<sup>19</sup> A change in the Raman spectrum after the hydrothermal reaction is clearly seen by the formation of two new peaks, which further confirmed the growth of MoS<sub>2</sub> over FSG. The inset of Figure 2b shows an optical image taken at the same location from which the Raman spectrum was acquired. Two sharp peaks at 376  $\text{cm}^{-1}$  (E<sup>1</sup><sub>2g</sub>) and 402  $\text{cm}^{-1}$

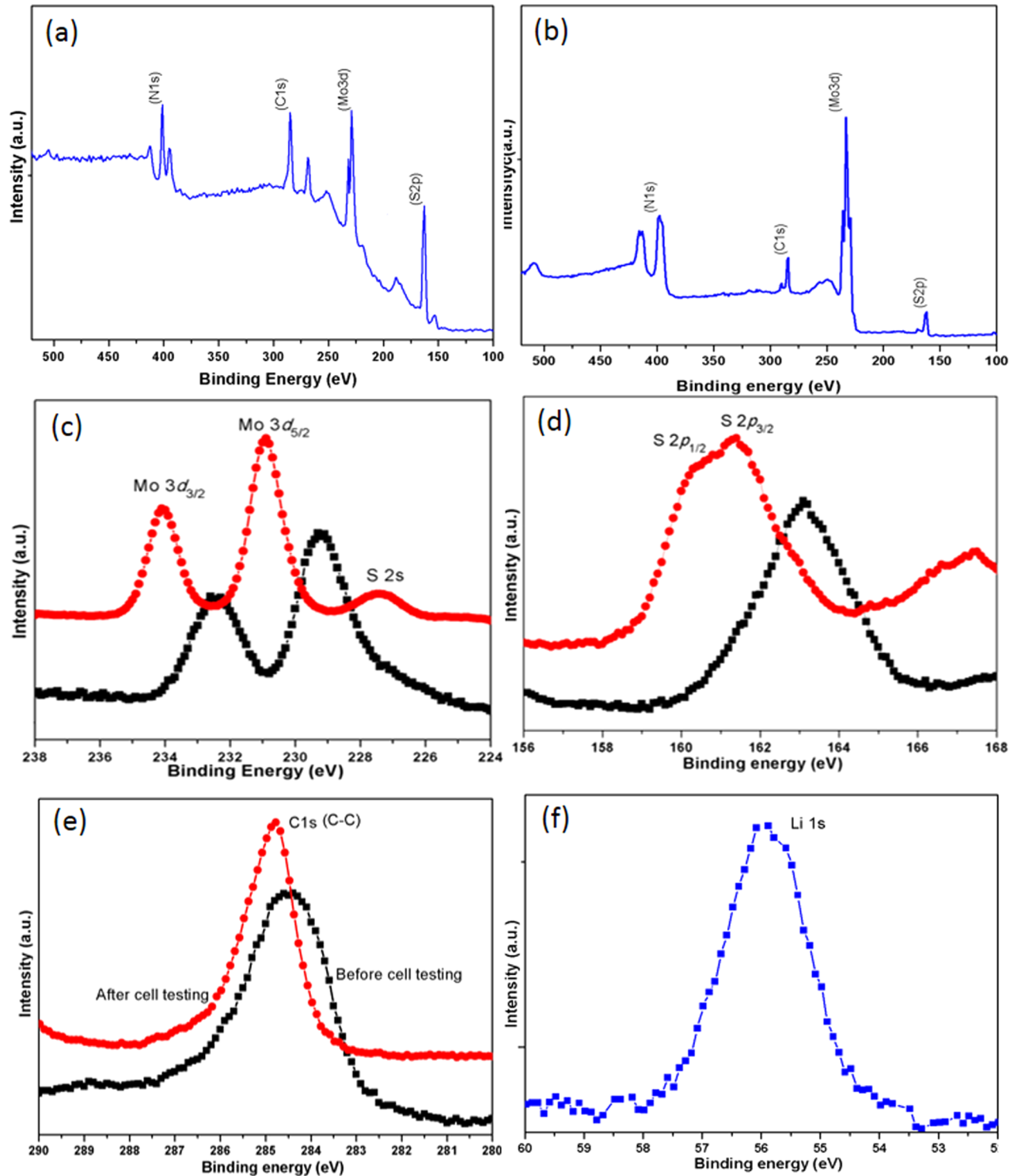


**Figure 3.** XPS survey spectra obtained for FSG/MoS<sub>2</sub> (a) before and (b) after cell testing. High-resolution XPS spectra acquired for the electrode materials before and after cell testing: (c) Mo 3d, (d) S 2p, (e) C 1s, and (f) Li 1s peaks after Li-intercalation into the MoS<sub>2</sub>/FSG.

(A<sub>1g</sub>), which correspond to first-order Raman vibrational modes within the S—Mo—S, were also observed (Figure 2c).<sup>20</sup> A more detailed view of the vibrational modes is presented in the inset of Figure 2c; two MoS<sub>2</sub> layers and the corresponding vibrations of bulk MoS<sub>2</sub> are displayed. The Raman spectrum obtained for the hybrid electrode materials (FSG/MoS<sub>2</sub>) is shown in Figure 2d along with an optical image of the electrode material after cell testing (inset). Structural changes in both the graphene and MoS<sub>2</sub> could be monitored from the Raman spectra of the FSG/

MoS<sub>2</sub> layers after various charge/discharge cycles. The shift in the G-band (1572 to 1579 cm<sup>-1</sup>) of graphene was attributed to charge transfer from lithium intercalation into the graphene layer.<sup>21</sup> The D-band decreased in intensity as defects on the FSG surface became saturated due to the formation of a solid electrolyte interface. New bands were observed at 150 and 205 cm<sup>-1</sup> after electrochemical lithium intercalation in the MoS<sub>2</sub>. These bands reflected the structural and electronic changes that occurred in the material as a result of electrochemical lithium

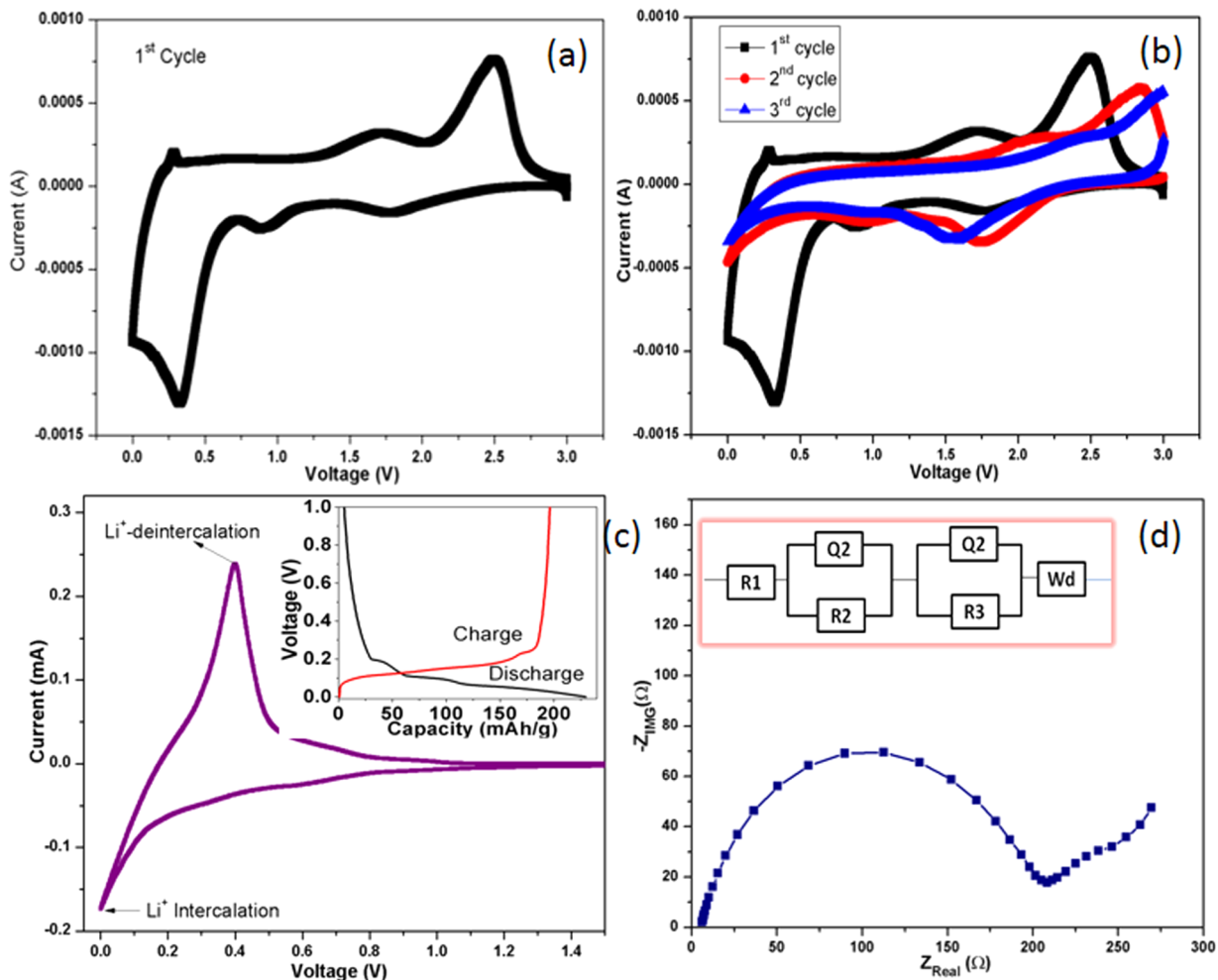


**Figure 4.** (a) Cyclic voltammograms obtained for a hybrid MoS<sub>2</sub>/FSG electrode used in a coin cell in a range of 0–3 V; the scan rate was 0.2 mV/s. (b) Cyclic voltammetry data acquired after three cycles at the same rate. (c) Cyclic voltammograms of thick free standing graphene without MoS<sub>2</sub> at 0.2 mV/s; the charge/discharge profile of the same structure is shown in the inset for comparison. (d) Impedance spectrum obtained for the coin cell after 20 cycles by applying a signal with an amplitude of 5.0 mV over a frequency range of 100 kHz to 0.01 Hz; the equivalent circuit model of the studied system is shown in the inset.

intercalation. The change in the Raman spectrum of the MoS<sub>2</sub> film reflected a structural transformation from trigonal to octahedral coordination, which was attributed to a process driven by a decrease in the electronic energy of the octahedral structure as electrons were transferred to the MoS<sub>2</sub> layer upon intercalation.<sup>22</sup> The chemical states of Mo, S, C, and Li were investigated by XPS before and after cell testing, and the acquired survey spectra are shown in panels a and b in Figure 3. The intense Mo<sup>4+</sup> 3d<sub>5/2</sub> and Mo<sup>4+</sup> 3d<sub>3/2</sub> components located at 229.3 and 232.5 eV, respectively, are displayed in Figure 3c; these features correspond to 2H-MoS<sub>2</sub>. Similarly, in the S 2p region of the XPS spectra, doublet peaks corresponding to 2H-MoS<sub>2</sub> S 2p<sub>1/2</sub> and S 2p<sub>3/2</sub> were observed at 163.4 and 162 eV, respectively (Figure 3d). The XPS results support the Raman and XRD findings and provide further confirmation that MoS<sub>2</sub> could be grown on the surface of a thick graphene film. XPS spectra were collected for FSG/MoS<sub>2</sub> after cell testing by etching the upper surface layer of the hybrid electrode in order to remove oxygen present on the surface. The effects of lithium intercalation on the Mo 3d and S 2p peaks are shown in Figure 3c and d, respectively. These features arose due to lithium intercalation into the MoS<sub>2</sub>. The Mo 3d<sub>5/2</sub> and 3d<sub>3/2</sub> peaks were shifted by 1.4 eV to higher binding energies. A similar trend was

observed in the XPS spectrum of S 2p, which was shifted by 1.2 eV. The C 1s spectra are shown in Figure 3e before and after cell testing. Before cell testing, the C 1s peak appeared at 284.3 eV, which corresponds to C–C bonding in the graphite lattice. The strong intensity of the C 1s XPS peak indicates that MoS<sub>2</sub> is not covering the entire surface of the thick freestanding graphene film. After cell testing, the C 1s peak shifted toward higher binding energies (284.8 eV) because of charge transfer from lithium to the carbon. These features correspond to the intercalated lithium compound Li<sub>x</sub>C<sub>6</sub> in the cell.<sup>23</sup> The XPS results revealed that lithium intercalation occurred in both MoS<sub>2</sub> and the graphitic carbon lattice. The presence of lithium ions in MoS<sub>2</sub> was also confirmed by XPS, as shown in Figure 3f. The Li 1s peak was observed at a binding energy of 55.9 eV, which represents a shift toward higher binding energies due to charge transfer to the MoS<sub>2</sub>, as the binding energy of metallic lithium is centred at 55 eV.<sup>23</sup> The XPS spectra acquired for the electrode materials before and after cell testing confirmed both the growth of MoS<sub>2</sub> over FSG and lithium insertion into the hybrid material.

The electrochemical performance of the as-synthesized FSG/MoS<sub>2</sub> samples as anodes was investigated using a half-cell configuration (hybrid electrode/separators/lithium foil). It is

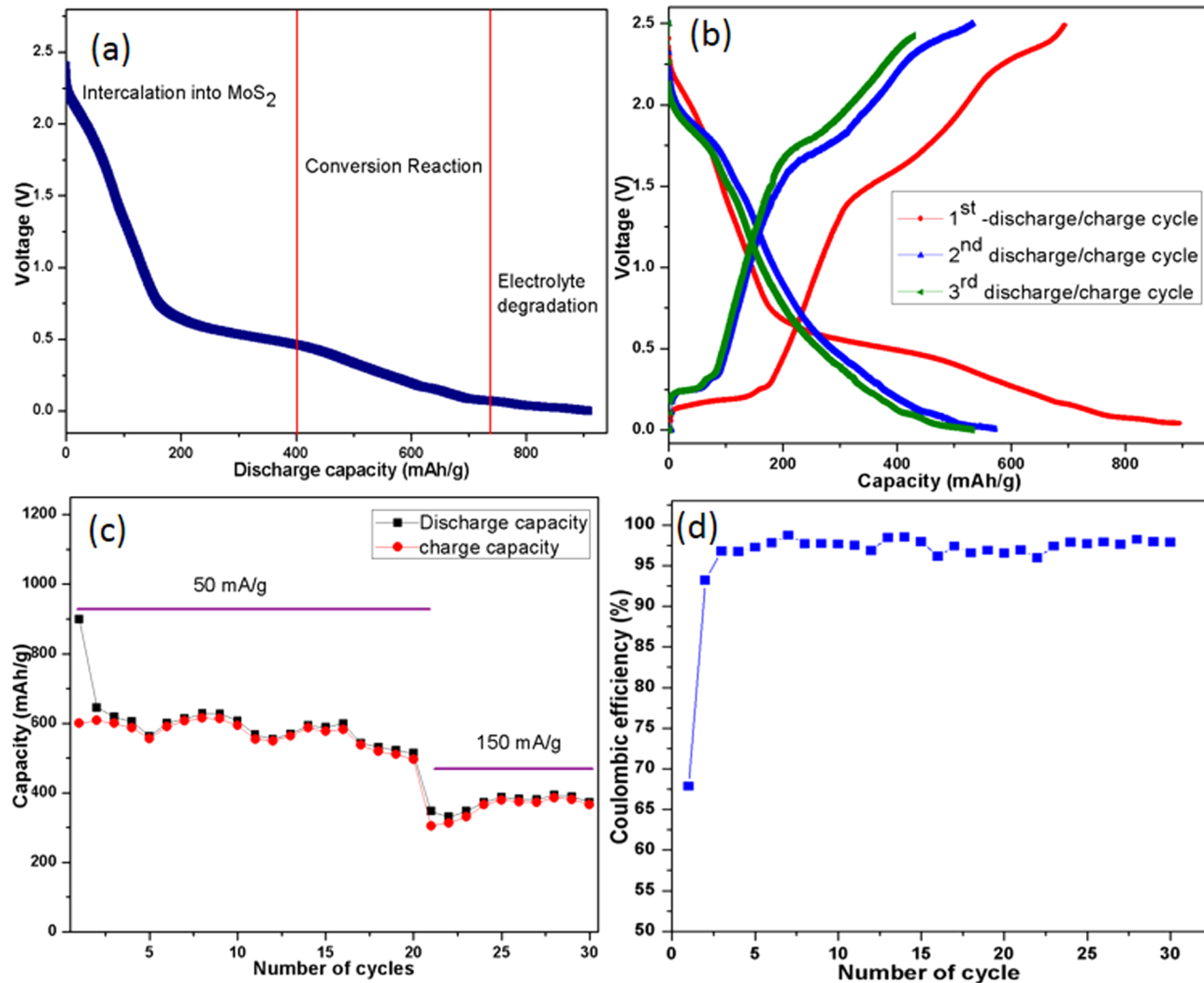


**Figure 5.** (a) Electrochemical performance of cell structure (FSG- $\text{MoS}_2$ /separator/Li) using coin cell. First discharge profile shows (b) different first and second charge and (c) discharge profile capacity of the cell with the number of cycles for two different current rates. (d) Coulombic Efficiency.

important to note that the FSG/ $\text{MoS}_2$  anodes employed in the half cell for electrochemical testing (cyclic voltammetry (CV) and charge/discharge) are used directly with no carbon additive, binder, or metal current collector. The loading weight (weight of active material) of  $\text{MoS}_2$  used in coin cell for electrochemical testing is 3 mg. CV testing was conducted on a fabricated electrode ( $\text{MoS}_2$ /FSG) at a scanning rate of 0.2 mV/s, and the obtained curve was compared with that acquired for FSG in the range of 0–3 V, as shown in Figure 4a–c. During the first discharge process, distinct peaks were observed at 0.9 and 0.3 V vs. Li/Li<sup>+</sup>. The peak at 0.9 V was related to the intercalation of lithium ions into the  $\text{MoS}_2$  layer, which leads to the formation of  $\text{Li}_x\text{MoS}_2$  species.<sup>21,22</sup> The peak at 0.3 V was characteristic of a conversion reaction from  $\text{Li}_x\text{MoS}_2$  to  $\text{Li}_2\text{S}^+\text{Mo}/\text{Li}_y^-$ . Before the start of this conversion reaction at 0.3 V, a broad shoulder indicative of the start of the conversion reaction was observed at 0.7 V. The peak at 0.3 V shifted toward lower voltages (as shown in Figure 4b) during consecutive cycles due to changes in the electronic environment by charge transfer. These changes could be attributed to lithium insertion into the  $\text{MoS}_2$  layers or at defect sites.<sup>23–27</sup> On the other hand, anodic sweeps revealed two broad peaks at 1.68 and 2.4 V vs. Li/Li<sup>+</sup>. The broad peak near 1.68 V may be

associated with a two-step lithium-ion de-intercalation process from Mo through a reduction reaction, whereas the sharp peak at 2.4 V vs. Li/Li<sup>+</sup> may be related to the oxidation of  $\text{Li}_2\text{S}$  to form sulfur.<sup>28</sup> During consecutive cycles, a peak at 1.75 V vs. Li/Li<sup>+</sup> was observed during the cathodic sweep and was attributed to the reaction of sulphur with lithium to yield  $\text{Li}_2\text{S}$ .<sup>28</sup> The cyclic voltammograms suggest a mechanism for the intercalation/de-intercalation of lithium into  $\text{MoS}_2$ . The obtained findings also served as confirmation that the hybrid electrode based on FSG/ $\text{MoS}_2$  was electrochemically stable. The CV data acquired from the pure FSG electrode is shown in Figure 4c for a comparison. The two peaks observed in the CV of pure FSG correspond to lithium intercalation and de-intercalation, which are typical characteristic peaks of a carbonaceous material. The difference in the shape of the CVs for FSG/ $\text{MoS}_2$  and thick FSG is clearly evident and may be ascribed to different lithium insertion mechanisms. The electrochemical performance of the FSG/ $\text{MoS}_2$  electrode was further explored by ac impedance measurements carried out after the 20th cycle; the results are shown in Figure 4d along with an equivalent circuit model of the hybrid electrode (inset). Here,  $R_1$  represents the internal resistance of the test cell,  $R_2$  and  $Q_2$  denote the resistance and constant phase element of the

solid electrolyte interface (SEI) film that formed on the electrode surface,  $R_3$  and  $Q_3$  are associated with the charge transfer resistance and constant phase element of the interface between the electrode and electrolyte, and  $W_d$  denotes the Warburg impedance that arises because of lithium insertion into the anode materials. The impedance spectrum is characterized by a well-defined semicircle at high and intermediate frequencies and a straight line inclined at a constant angle relative to the real axis at low frequencies. The high-frequency semicircle corresponds to the resistance of the SEI film, while the semicircle in the medium-frequency region represents the charge-transfer resistance at the electrode/electrolyte interface. The inclined line is associated with lithium diffusion within the hybrid electrode materials.<sup>29</sup> After fitting the impedance spectrum, the internal resistance value was found to be  $5.2\ \Omega$ , whereas the SEI film resistance and charge transfer resistance of the FSG/MoS<sub>2</sub> electrode are  $28$  and  $196\ \Omega$ , respectively. These values are higher than those reported for FSG/MoS<sub>2</sub> composites,<sup>24,29</sup> which may in part explain the higher capacity of the latter. The impedance spectrum of MoS<sub>2</sub> electrode using binder and conducting agent on copper foil has also been acquired in order to compare with MoS<sub>2</sub>/FSG hybrid electrode in coin cell. The internal resistance value was found to be  $3\ \Omega$ , whereas the SEI film resistance and charge transfer resistance of the FSG/MoS<sub>2</sub> electrode are  $8.5$  and  $28\ \Omega$ , respectively. These values are lower than the FSG/MoS<sub>2</sub> hybrid electrode. A higher impedance of MoS<sub>2</sub>/FSG hybrid electrode is mainly expected because of the resistance at interface of MoS<sub>2</sub> and FSG as compared with MoS<sub>2</sub> using binder and conducting agent. However, the material used in the present study is advantageous in that it is freestanding and contains no additives. Considering that additive- and current collector-free hybrid anode materials are beneficial for LIBs when compared to conventional electrodes, we investigated the lithium storage properties of the as-prepared MoS<sub>2</sub>/FSG freestanding film when utilized as an anode. The performance of the MoS<sub>2</sub>/FSG structure vs. Li/Li<sup>+</sup> during charge/discharge cycles and over multiple cycles was examined along with the columbic efficiency of the cell; the results are shown in Figure 5a–d. Figure 5a shows the first discharge profile of the hybrid electrode vs. Li/Li<sup>+</sup>. The electrode displayed two voltage plateaus at  $0.9$  and  $0.6$  V vs. Li/Li<sup>+</sup>. The first plateau at  $0.9$  V was associated with the formation of Li<sub>x</sub>MoS<sub>2</sub> ( $0 < x < 4$ ) via lithium intercalation into the interlayer spacing of MoS<sub>2</sub>, as described by the reaction MoS<sub>2</sub> +  $x$ Li<sup>+</sup> +  $ne^- \rightarrow$  Li<sub>x</sub>MoS<sub>2</sub>.<sup>28,30</sup> The long plateau at  $0.6$  V was attributed to a conversion reaction related to the reduction of MoS<sub>2</sub> to Mo metal and the formation of Li<sub>2</sub>S according to reaction MoS<sub>2</sub> +  $2x$ Li<sup>+</sup> +  $2xe^- \rightarrow$  Mo +  $x$ Li<sub>2</sub>S.<sup>26</sup> The plateau at lower voltages (below  $0.2$  V) is attributed to the intercalation of lithium between graphene planes and the formation of LiC<sub>x</sub> ( $0 < x < 6$ ), as the surface of the FSG is not completely covered by MoS<sub>2</sub>. Degradation of the electrolyte at the electrode surface also contributes to the appearance of the plateau at lower voltages. The charge profile, which indicates lithium de-intercalation from FSG/MoS<sub>2</sub>, is shown in Figure 5b. The first charge profile shows a voltage plateau at  $2.1$  V, which was related to the oxidation of Li<sub>2</sub>S in sulphur.<sup>21</sup> Figure 5b displays the first three charge and discharge curves of FSG/MoS<sub>2</sub> vs. Li/Li<sup>+</sup>. The first discharge and charge capacities of FSG/MoS<sub>2</sub> were  $899$  and  $614$  mAh/g, respectively, resulting in a columbic efficiency of  $68\%$ . These values were significantly higher ( $525$ – $600$  mAh/g) than those obtained for bulk or exfoliated MoS<sub>2</sub>.<sup>26</sup> The discharge capacities

during the second and third cycles were  $580$  and  $535$  mAh/g, respectively, and the values remained nearly constant. Consequently, a columbic efficiency of  $97\%$  (Figure 5d) was maintained up to the 30th cycle. The higher first discharge capacity in the FSG/MoS<sub>2</sub> hybrid electrode was attributed to the large surface area of the MoS<sub>2</sub> layer, which is composed of vertically aligned flower-like structures. These structures increased the surface area available to the electrolyte and offered easy access for lithium insertion. To compare the performance of binder-free electrode (MoS<sub>2</sub>/FSG), we have shown the first charge/discharge profile of MoS<sub>2</sub> powder in Figure S3a in the Supporting Information. The electrode was fabricated by adding binder and carbon black and coating over copper film. The coin cell using this electrode has been tested at same current, which shows a discharge capacity and charge capacity about  $840$  and  $515$  mAh/g, respectively. This value is a little lower than that of the binder-free electrode. Figure 5c shows the rated capacity of the FSG/MoS<sub>2</sub> hybrid electrode at two different current rates. A capacity of  $498$  mAh/g was obtained after the 20th cycle at a current density of  $50$  mA/g, whereas a capacity of  $385$  mAh/g was obtained after the 30th cycle at  $150$  mA/g. Good capacity retention was observed as the current density was increased by a factor of three, indicating good rate performance. The columbic efficiency of the electrode vs. Li/Li<sup>+</sup> was  $68\%$  for the first cycle when the cell was operated at a current density of  $150$  mA/g. The efficiency improved during the second cycle and, in subsequent cycles, reached a constant value ( $97\%$ ) that was similar to the efficiency obtained when the cell was operated at a current density of  $50$  mA/g. The inset of Figure 4c shows the first discharge/charge profile of the thick FSG before MoS<sub>2</sub> growth. The first discharge capacity of the FSG was found to be  $240$  mAh/g. Lithium intercalation in the FSG begins below  $0.19$  V, which is a characteristic feature of carbon-based anode materials. The difference in the first discharge profiles of FSG and FSG/MoS<sub>2</sub> is clearly evident, as lithium intercalation takes place at different voltages. Despite the absence of a binder and carbon black, the reversible capacity of the hybrid electrode stabilized after a few cycles at the two different current densities ( $50$  and  $150$  mA/g). The additive- and current-collector-free hybrid electrode exhibited good capacity and stability for use in LIBs. Although the hybrid electrode (FSG/MoS<sub>2</sub>) employed in the present work had a lower capacity than that measured for composites of MoS<sub>2</sub> and graphene or graphene oxide,<sup>31,32</sup> the morphology and particle size of the hybrid electrode described here could be controlled and the introduction of impurities may be avoided during the synthesis of graphene oxide. The freestanding and additive-free (FSG/MoS<sub>2</sub>) hybrid structure may also be useful as an electrode material in flexible energy storage devices.

## CONCLUSION

In summary, we described a two-step (CVD and hydrothermal) route to produce hybrid anode materials without the need for additives, binders, or metallic current collectors. These anodes can be used directly in a cell with no post treatment, which may eliminate the need for additional LIB safety features. MoS<sub>2</sub> nanostructures can be grown directly on a thick graphene surface as an alternative current collector. The highly conductive and freestanding thick graphene film covered with MoS<sub>2</sub> has a large surface area that increases the electrode surface area available for electrolyte interactions. Furthermore, good adhesion exists between the MoS<sub>2</sub> and FSG. The thick

FSG film serves multiple functions: a mechanical support for MoS<sub>2</sub>, a current collector delivering electrons, and as a lithium-storage material. The synthesis method adopted in the present study can be extended to other transition metal oxides and chalcogenides for the fabrication of high-performance electrodes. These structures may advance the utilization of free-standing thick graphene films and additive-free electrodes in super capacitors and other energy storage and conversion devices for the development of a new generation of thin, bendable, and flexible devices.

## EXPERIMENTAL DETAILS

Thick graphene films have been grown on Ni metal foil substrate of thickness 25 μm using the chemical vapor deposition (CVD) process. The substrates were first placed away from the heating zone of tubular furnace and temperature was raised up to 1000 °C in a steady flow of argon with a flow rate of 100 sccm. The polycrystalline Ni substrates were loaded into the centre of the tube furnace when the temperature rose up to 1000 °C. The graphene growth started with decomposition of methane at a flow rate of 400 and hydrogen at 150 sccm for 4 h. The carbon source decomposed which dissolved and diffused into the nickel layer and deposited on both sides of the nickel to form a thick graphene film upon fast cooling. After etching away the nickel, thick free standing graphene (FSG) film was obtained. The thick FSG was used to grow MoS<sub>2</sub> over it using the hydrothermal method. Ammonium molybdate ((NH<sub>4</sub>)<sub>2</sub>MoO<sub>4</sub>) and thiourea (CS (NH<sub>2</sub>)<sub>2</sub>) (in 1:4 molar ratio) and hydrazine (NH<sub>2</sub>NH<sub>2</sub>) were dissolved in water and hydrochloric acid (HCl) was added to the solution adjusting the pH to 3. The resulting solution was transferred into a 100 ml Teflon cylinder, sealed inside the stainless steel vessel where hydrothermal reaction was carried out at the 200 °C for 36 h. After cooling, the samples were taken out and washed with distilled water and ethanol successively.

XRD analysis was performed on an X-ray diffractometer with monochromatized CuKα radiation ( $\lambda = 0.15405$  nm). Different metal–sulfur vibration modes were obtained using a Raman spectrometer having 532 nm lasers at 10 mW power. FE-SEM was used to study the surface morphology of the samples. Further investigations were done by XPS to study the binding energies of various elements present and the formation of MoS<sub>2</sub>.

Electrochemical testing was carried out by using a coin cell fabricated in the configuration of Li/separator/(FSG-MoS<sub>2</sub>). Cells were fabricated in an argon-filled glove box with oxygen and moisture level less than 1 ppm. The Li metal foil was used as the counter electrode and 1M LiPF<sub>6</sub> in EC/DEC (1:1 by volume) as the electrolyte. The polypropylene film was used as a separator between the electrodes which is an insulator for electrons but lithium ions can diffuse through it. Cyclic voltammetry (CV) profile was obtained by measuring current-voltage response at a scan rate of 0.2 MV/s within the voltage window of 0.01–2.5 V. The electrochemical charge/discharge was performed in the galvanostatic mode at two different current densities 50 and 150 mA/g for 30 cycles. All the electrochemical measurements were carried out at the room temperature.

## ASSOCIATED CONTENT

### Supporting Information

Additional FESEM image of FSG after MoS<sub>2</sub> and mechanical bending of FSG vs resistance change with bending radius and inset show the photograph during. Additional Raman spectra of pure FSG before and after MoS<sub>2</sub> and EDAX. Additional discharge profile and impedance spectrum of MoS<sub>2</sub> using binder. This material is available free of charge via the Internet at <http://pubs.acs.org>.

## AUTHOR INFORMATION

### Corresponding Authors

\*E-mail: ahnj@yonsei.ac.kr.  
\*E-mail: lutts@skku.edu.

### Notes

The authors declare no competing financial interest.

## ACKNOWLEDGMENTS

This work was supported by the Brain Korea (BK) 21 plus program, Basic Research Program (2012R1A2A1A03006049 and 2009-0083540), and the Global Frontier Research Center for Advanced Soft Electronics (2013M3A6A5073170) through the National Research Foundation of Korea (NRF), funded by the Ministry of Education, Science and Technology.

## REFERENCES

- (1) Fischer, J. E.; Kim, H. J. Neutron Scattering Studies of Dilute Stage I Li-graphite Intercalation Compound: Elastic Interactions, Phase Transition and Phase Diagram. *Synth. Met.* **1988**, *23*, 121–126.
- (2) Choi, H.-J.; Jung, S.-M.; Seo, J.-M.; Chang, D.W.; Dai, L.; Baek, J.-B. Graphene for Energy Conversion and Storage in Fuel Cells and Supercapacitors. *Nano Energy* **2012**, *1*, 534–551.
- (3) Chaohe, X.; Binghui, X.; Yi, G.; Zhigang, X.; Jing, S.; Zhao, X. S. Graphene-based Electrodes for Electrochemical Energy Storage. *Energy Environ. Sci.* **2013**, *6*, 1388–1414.
- (4) Yoo, E. J.; Kim, J.; Hosono, E.; Zhou, H.-S.; Kudo, T.; Honma, I. Large reversible Li storage of Graphene Nanosheet Families for Use in Rechargeable Lithium Ion Batteries. *Nano Lett.* **2008**, *8*, 2277–2282.
- (5) Chen, J.; Liu, Y.; Minett, A. I.; Lynam, C.; Wang, J.; Wallace, G. G. Flexible, Aligned Carbon Nanotube/Conducting Polymer Electrodes for a Lithium Ion Battery. *Chem. Mater.* **2007**, *19*, 3595–3597.
- (6) Zhao, X.; Hayner, C. M.; Kung, H. H. Flexible Poly Graphene Paper Electrodes With Enhanced Rate Capability for Energy Storage Applications. *ACS Nano* **2011**, *5*, 8739–8749.
- (7) Gwon, H.; Kim, H.-S.; Lee, K. U.; Seo, D.-H.; Park, Y. C.; Lee, Y.-S.; Ahn, B. T.; Kang, K. Flexible Energy Storage Devices Based Graphene Paper. *Energy Environ. Sci.* **2011**, *4*, 1277–1283.
- (8) Yang, S. B.; Feng, X.; Zhi, L.; Cao, Q.; Maier, J.; Mullen, K. Nanographene-constructed Hollow Carbon Spheres and Their Favorable Electroactivity with Respect to Lithium Storage. *Adv. Mater.* **2010**, *22*, 838–842.
- (9) Ji, H.; Zhang, L.; Pettes, M.T.; Li, H.; Chen, S.; Shi, L.; Piner, R.; Ruoff, R. S. Ultrathin Graphite Foam: a Three Dimensional Conductive Network for Battery Electrodes. *Nano Lett.* **2012**, *12*, 2446–2451.
- (10) Gong, Y.; Yang, S.; Liu, Z.; Ma, L.; Vajtai, R.; Ajayan, P. M. Graphene-network-backboned Architectures for High-performance Lithium Storage. *Adv. Mater.* **2013**, *25*, 3979–3984.
- (11) Li, N.; Chen, Z.; Ren, W.; Li, F.; Cheng, H.-M. Flexible Graphene-based Lithium Ion Batteries with Ultrafast Charge and Discharge rates. *Proc. Natl. Acad. Sci. U.S.A.* **2012**, *109*, 17360–17365.
- (12) Reddy, A. L. M.; Srivastava, A.; Gowda, S. R.; Gullapalli, H.; Dubey, M.; Ajayan, P. M. Synthesis of Nitrogen-doped Graphene Films for Lithium Battery Application. *ACS Nano* **2010**, *4*, 6337–6342.
- (13) Zhang, C.; Wang, Z.; Guo, Z.; Lou, X. W. Synthesis of MoS<sub>2</sub>-C One-dimensional Nanostructures with Improved Lithium Storage Properties. *ACS Appl. Mater. Interfaces* **2012**, *4*, 3765–3768.
- (14) Pham, V. H.; Kim, K.-H.; Jung, D.-W.; Singh, K.; Oh, E.-S.; Chung, J. S. Liquid Phase Co-Exfoliated MoS<sub>2</sub>-graphene Composite as Anode Materials for Lithium Ion Batteries. *J. Power Sources* **2013**, *244*, 280–286.
- (15) Sun, Y.; Hu, X.; Luo, W.; Huang, Y. Graphene Nano-architectures and Their Application as a High-performance Anode Material for Lithium-ion Batteries. *ACS Nano* **2011**, *5*, 7100–7107.
- (16) Ding, S.; Chen, J. S.; Lou, X.W. (David). Glucose-Assisted Growth of MoS<sub>2</sub> Nanosheets on CNT Backbone for Improved Lithium Storage Properties. *Chem.—Eur. J.* **2011**, *17*, 13142–13145.

- (17) Chhowalla, M.; Shin, H. S.; Eda, G.; Li, L.-J.; Loh, K.P.; Zhang, H. The Chemistry of Two-dimensional Layered Transition Metal Dichalcogenide Nanosheets. *Nat. Chem.* **2013**, *5*, 263–275.
- (18) Tenne, R.; Margulis, L.; Genut, M.; Hodes, G. Polyhedral and Cyclindrical Structure of Tungsten Disulphide. *Nature* **1992**, *360*, 444–446.
- (19) Ferrari, A. C.; Meyer, J. C.; Scardaci, V.; Casiraghi, C.; Lazzeri, M.; Mauri, F.; Mauri, S.; Jiang, D.; Novoselov, K. S.; Roth, S.; Geim, A. K. Raman Spectrum of Graphene and Graphene layers. *Phys. Rev. Lett.* **2006**, *97* (187401), 1–4.
- (20) David, L.; Bhandavat, R.; Singh, G. MoS<sub>2</sub>/Graphene Composite Paper for Sodium-Ion Battery Electrodes. *ACS Nano* **2014**, *8*, 1759–1770.
- (21) Sen, U. K.; Mitra, S. High Rate and High-energy-density Lithium-ion Battery Anode Containing 2D MoS<sub>2</sub> Nanowall and Cellulose Binder. *ACS Appl. Mater. Interfaces* **2013**, *5*, 1240–1247.
- (22) Gogotsi, Y.; Simon, P. True performance metrics in electrochemical energy storage. *Science* **2011**, *334*, 917–918.
- (23) Rana, K.; Dogu, G. K.; Sen, H. S.; Boothroyd, C.; Gulseren, O.; Bengu, E. Analysis of Charge Transfer for *in situ* Li intercalated Carbon Nanotubes. *J. Phys. Chem. C* **2012**, *116*, 11364–11369.
- (24) Chang, K.; Chen, W. L-cysteine-assisted Synthesis of Layered MoS<sub>2</sub>/graphene Composites with Excellent Electrochemical Performances for Lithium Ion Batteries. *ACS Nano* **2011**, *5*, 4720–4728.
- (25) Lei, D.; Zhang, M.; Qu, B.; Chen, L.; Wang, Y.; Zhang, E.; Xu, Z.; Li, Q.; Wang, T.  $\alpha$ -Fe<sub>2</sub>O<sub>3</sub> Nanowall Arrays: Hydrothermal Preparation, Growth Mechanism and Excellent Rate Performances for Lithium Ion Batteries. *Nanoscale* **2012**, *4*, 3422–3426.
- (26) Julien, C.M. Lithium intercalated Compounds Charge Transfer and Related Properties. *Mater. Sci. Eng., R* **2003**, *40*, 47–102.
- (27) Xiao, J.; Wang, X.; Yang, X.-Q.; Xun, S.; Liu, G.; Koech, P. K.; Liu, J.; Lemmon, J. P. Electrochemically Induced High Capacity Displacement Reaction of PEO/MoS<sub>2</sub>/graphene Nanocomposites with Lithium. *Adv. Funct. Mater.* **2011**, *21*, 2840–2846.
- (28) Ding, S.; Zhang, D.; Chen, J. S.; Lou, X.W. (David).Facile Synthesis of Hierarchical MoS<sub>2</sub> Microspheres Composed of Few-layered Nanosheets and Their Lithium Storage Properties. *Nanoscale* **2012**, *4*, 95–98.
- (29) Cao, X.; Shi, Y.; Shi, W.; Rui, X.; Yan, Q.; Kong, J.; Zhang, H. Preparation of MoS<sub>2</sub>-coated Three-Dimensional Graphene Networks for High-Performance Anode Material in Lithium-Ion Batteries. *Small* **2013**, *9*, 3433–3438.
- (30) Wang, Q.; Wen, Z.; Jeong, Y.; Choi, J.; Lee, K.; Lee, J. Li-driven Electrochemical Properties of WO<sub>3</sub> Nanorods. *Nanotechnology* **2006**, *17*, 3116 –3120.
- (31) Hwang, H.; Kim, H.; Cho, J. MoS<sub>2</sub> Nanoplates Consisting of Disordered Graphene-like Layers for High Rate Lithium Battery Anode Materials. *Nano Lett.* **2011**, *11*, 4826–4830.
- (32) Yu, H.; Ma, C.; Ge, B.; Chen, Y.; Xu, Z.; Zhu, C.; Li, C.; Ouyang, Q.; Gao, P.; Li, J.; Sun, C.; Qi, L.; Wang, Y.; Li, F. Three-dimensional Hierarchical Architectures Constructed by Graphene/MoS<sub>2</sub> Nanoflake Arrays and Their Rapid Charging/discharging Properties as Lithium-ion Battery Anode. *Chem.—Eur. J.* **2013**, *19*, 5818–5823.